Significance of powder feedstock characteristics in defect suppression of additively manufactured Inconel 718

Yufan Zhao [a], Kenta Aoyagi [a, *], Yohei Daino [a, 1], Kenta Yamanaka [a], Akihiko Chiba [a]

[a] *Institute for Materials Research, Tohoku University, 2-1-1 Katahira, Aoba-ku, Sendai 980-8577, Japan*

* Corresponding author. Ph.D.; Tel.: +81 022 2152118.

E-mail address: k.aoyagi@imr.tohoku.ac.jp (K. Aoyagi).

Abstract

The characteristics of powder applied in electron beam powder-bed fusion (EB-PBF) play a vital role in the process stability and final part performance. We use two types of Inconel 718 alloy powders for experiments, namely, (i) imperfect spherical and (ii) spherical powders. They are different in geometry and built-in defect because of different powder fabrication techniques. The forming qualities concerning surface topography, density, and internal defect of the EB-PBF-built IN718 samples prepared using two types of powders are characterized under the same processing conditions. In particular, the forming qualities of the samples built with each kind of powder, under the optimal process condition, derived by a machine learning method, are further compared. Notably, different powder geometries with different surface features inevitably affect the heat transfer during melting. The significance of powder feedstock characteristics in defect suppression is clarified with the aid of numerical simulations. Under the processing conditions of the present study, compared to those of spherical powders, imperfect spherical powders exhibit low energy absorption rate and low thermal conductivity, making them more likely to evoke lack–of–fusion and excessive melting under low and high energy conditions, respectively. Thus, spherical powders have a broader process window in ensuring a higher density and smoother surface than that of imperfect spherical powders. Moreover, the high cooling and solidification rates in the sample built with spherical powders result in the suppression of the interdendritic void formation.

[1] Present address: JEOL Ltd., 3-1-2 Musashino, Akishima, Tokyo 196-8558, Japan

Keywords: Electron beam powder-bed fusion; Powder feedstocks; Inconel 718; Forming quality; Defect suppression.

1. Introduction

Electron beam powder-bed fusion (EB-PBF) has been recognized as an appropriate additive manufacturing (AM) technique to produce various metallic components with near-net-shape [1][2]. The EB-PBF utilizes an electron beam to melt a metallic powder feedstock and produces components with complex geometries in a layer-by-layer manner. Recent researches [3][4][5] have suggested that the characteristics of the metallic powder feedstock played a significant role in the defect suppression and, consequently, in the final performance of the AM-built components. Based on such concern, researchers have committed to figure out how raw material powder and which kind of its critical features affect the forming quality and performance of the PBF-built parts. Aboulkhair et al. [6] demonstrated that the variability of AlSi10Mg powder in terms of morphology, surface characteristics, composition, and size distribution affected the defect formation in laser-PBF-built parts. Karlsson et al. [7] investigated the utilization of two different powders of Ti–6Al–4V with different size fractions in the EB-PBF process. They found that the surface appearances were different for the samples fabricated using different powder sizes. The studies conducted by Panwisawas et al. [8] and Tillmann et al. [9] indicated that the trapped gas in feedstock powder acted as a source of pore formation in laser-PBF-built samples. Cunningham et al. [10] claimed that the degree of porosity in the EB-PBF-built parts was correlated with the pores in the feedstock powder.

Nickle-based superalloy Inconel 718 that is widely applied in aircraft industries has attracted considerable interest from the AM researchers [11][12][13][14] for years, due to its exceptional material properties including high strengths, creep-rupture resistance at elevated temperatures (about 700 °C), and excellent corrosion resistance. The characteristics of powder applied in PBF process play a vital role in the process stability and final part performance. In particular, powder morphology makes an essential impact on powder flowability and, consequently, on the spreading uniformity of powder layer during PBF processing [15][16]. Notably, as powder particles undergo a thermal interaction with an electron beam, the surface characteristics of the powder layer correlated to the powder morphology will inevitably influence the heat transfer and consolidation process. There is a

demand to know exactly how the powder characteristics affect the forming quality of the EB-PBF-built Inconel 718 components.

In the present study, the Inconel 718 samples were fabricated using (i) imperfect spherical and (ii) spherical powders, under the same process parameters domain determined by uniform experimental design. The forming qualities were characterized in terms of surface topography, density, and internal defect. Then, based on the relationship between the processing parameters and the forming qualities obtained above, the optimal parameters corresponding to each kind of powder stock were determined using a machine learning method. The samples processed with the optimal parameters were also evaluated and characterized. Meanwhile, mesoscale numerical simulations were applied to analyze the fusion process of powder layers composed of two types of powders, thereby clarifying the significance of powder characteristics in defect suppression of EB-PBF-built Inconel 718.

2. Methodology

2.1 Materials and EB-PBF processing

We use two types of Inconel 718 alloy powders for experiments, namely, (i) imperfect spherical powders and (ii) spherical powders fabricated by gas atomization (GA) and plasma-rotating electrode process (PREP), respectively. During the GA process, the molten metal is fed through a nozzle and then atomized into particles by a jet stream of inert gas. Small particles fly back to attach to partially melted particles, easily producing imperfect spherical powders with satellite particles and a relatively large surface area [17]. Gas entrapment during solidification contributes to the pore formation in these powders [18]. Such entrapped pore can increase the porosity in the AM-built components [19]. During the PREP process, through the melting of a rotating metal bar by a plasma arc, the fine molten droplets are thrown out under the action of high-speed centrifugal force and then solidified into powder particles, producing spherical powders with considerably low porosity [20][21]. The (i) imperfect spherical and (ii) spherical powders of Inconel 718 were provided by Sanyo Special Steel Co., Ltd. (Himeji, Japan) and Fukuda Metal Foil & Powder Co., Ltd. (Kyoto, Japan), respectively. Table 1 shows the chemical compositions of the powders measured by ICP-AES. The morphologies and particle size distributions (PSDs) of powders are shown in Fig. 1. Two types of powders have

almost the same range and mean values (78.7 μm for imperfect spherical powders; 83.5 μm for spherical powders) in particle diameter, which minimizes the effect of PSD on the result. In the imperfect spherical powders, particle adhesion with distorted shape and satellites present, and inner pore (Fig. 1(c)) can be observed. The spherical powders (Fig. 1(b) and (d)) possess high sphericity and smooth surface (Fig. 1(a) and (c)).

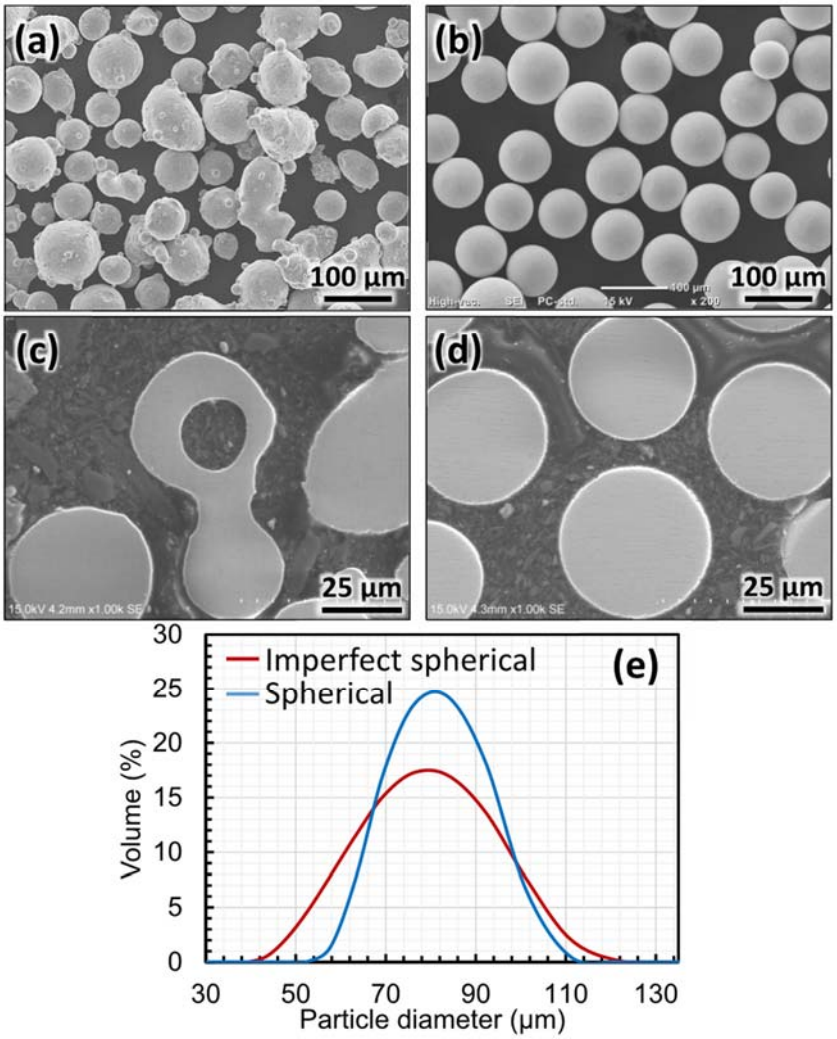

Fig. 1. (a)(c)Imperfect spherical and (b)(d)spherical powders of Inconel 718. (e)Both types of powders have similar ranges in particle size distribution.

Table 1 Chemical composition (mass%) of (i) imperfect spherical and (ii) spherical powders.

	Ni	Cr	Mo	Al	Ti	Nb	Mn	C	N	Fe
(i)	52.43	18.90	3.05	0.49	0.89	4.99	0.15	0.039	0.072	Bal.
(ii)	52.60	18.60	3.00	0.65	0.99	5.20	0.05	0.045	0.006	Bal.

The Inconel 718 cuboid samples with dimensions of 15 mm × 15 mm × 20 mm (Fig. 2) were produced on a SUS304 substrate using an EB-PBF machine developed by Technology Research Association for Future Additive Manufacturing (TRAFAM). The samples were fabricated using the imperfect spherical and spherical powders under the same process conditions, i.e., electron beam power (P) and beam scan speed (V). The P ranged between 120 and 1140 W, and the V ranged between 135 and 1325 mm/s. The process parameters for the building are shown in Table. 2; they were organized in two batches depending on uniform experimental design [22] so that parameters P and V were uniformly scattered on the experimental domain. The line offset was 0.2 mm for all of the samples. The preheating temperatures were kept at 1273 K to avoid powder smoke. An XY-scanning strategy, in which the bi-directional scanning direction was rotated by 90° in each 75 μm layer, was applied.

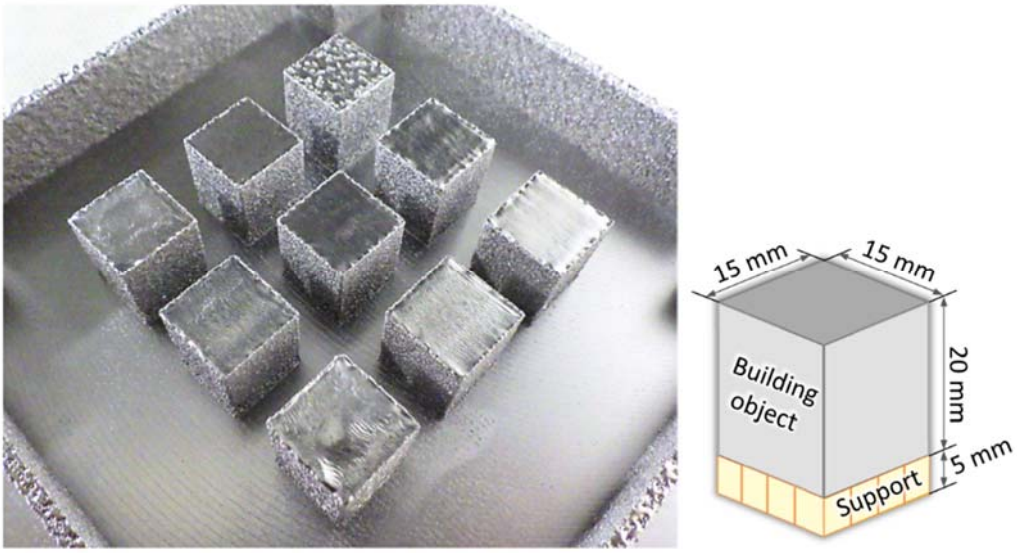

Fig. 2. One batch of Inconel 718 cuboid samples with dimensions of 15 mm ×15 mm ×20 mm fabricated on a SUS304 substrate.

2.2 Materials characterization

The sample surface topography displayed by stereoscopic imaging was measured using a Keyence® VR-3200 wide-area 3D measurement system. The densities of the as-built samples were evaluated through the Archimedes method. For observing the internal defects, the cuboid samples were cut along the building direction (z-axis) using a wire electric discharge machine, and then the

sectioned samples were ground and polished by standard metallographic techniques. Scanning electron microscopy (SEM) was utilized to observe the cross sections.

Table 2 Processing condition of each sample in the two batches of fabrications.

Batch No.	Sample No.	Beam current (mA)	Scan speed (mm/s)	Volume energy (J/mm^3)
Batch 1	1	4	1255	12.749
	2	6	1045	22.967
	3	9	1115	32.287
	4	3	345	34.783
	5	5	555	36.036
	6	13	1325	39.245
	7	8	695	46.043
	8	11	905	48.618
	9	18	1185	60.759
Batch 2	10	2	835	9.581
	11	16	975	65.641
	12	14	765	73.203
	13	10	485	82.474
	14	19	625	121.6
	15	7	205	136.585
	16	15	415	144.578
	17	17	275	247.273
	18	12	135	355.556

2.3 Numerical simulations

A particle-based discrete element method (DEM) model was utilized to simulate the powder bed generation. The DEM allows the modeling of a collection of particles that interact at the contact points following a governing force-displacement relationship [23]. The powder layer formation by raking in EB-PBF was simulated using the open-source software Yade [24]. The DEM simulation

was followed by the computational thermo-fluid dynamics (CtFD) simulation of single-track melting. A 3D transient model of molten pool dynamics was developed using a commercial Multiphysics-modeling program—Flow 3D® [25]. Detailed descriptions of the modeling physics, physical properties of the materials, necessary parameters and coefficients, and modeling validations are available in the previous studies [26][27].

3. Results

3.1 Surface topography and density

The amount of energy input can be expressed in terms of volume energy for the parts with the same dimensions [28]. As shown in Table. 2, the applied volume energy increased from sample No. 1 (12.749 J/mm^3) to sample No. 9 (60.759 J/mm^3) in Batch 1 and from sample No. 10 (9.581 J/mm^3) to sample No. 18 (355.556 J/mm^3) in Batch 2. Fig. 3 shows the three-dimensional surface topographical images of the two batches processed with both types of powders. The samples No. 16, 17, and 18 were not successfully manufactured due to excessive energy input.

The representative Batch 1 was taken as the demonstration. Under low energy conditions, the samples No. 1 and 2, built with the imperfect spherical powders, exhibited porous morphological features of a lack–of–fusion, with large voids making their appearance. Inadequate penetration of molten pool that is directly related to powder properties and insufficient energy input gives rise to lack–of–fusion [29]. Only sample No. 1 built with the spherical powders possessed such kind of potholed surface. Under high energy conditions, the samples No. 7, 8, and 9, built with the imperfect spherical powders, showed uneven surface due to the excessive melting. The excessive melting caused by overheating or slow heat dissipation [30] can generate an oversized molten pool that exists for an extended period. Under the action of surface tension, the solidified surface shows protrusions and depressions. By contrast, for the samples built with the spherical powders, the surface unevenness caused by excessive melting appeared until the volume energy increased to 60.759 J/mm^3 (sample No. 9).

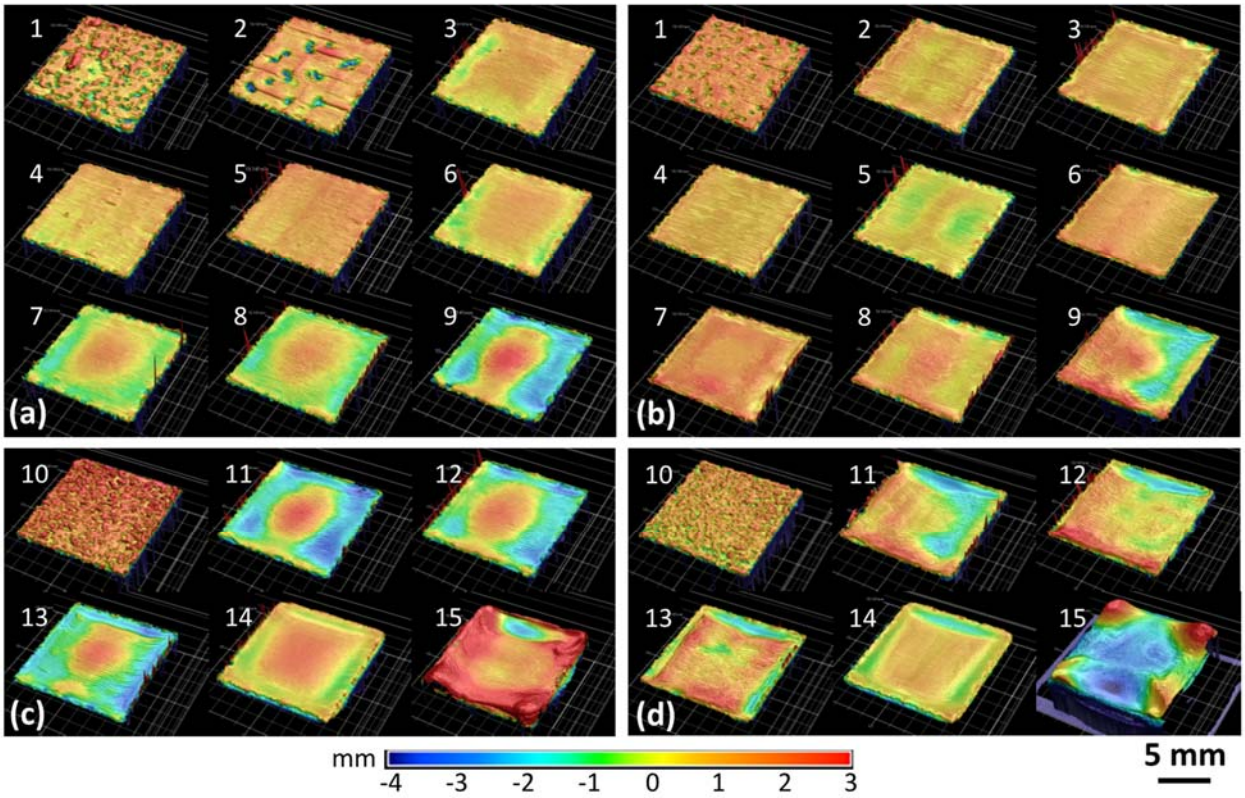

Fig. 3. Three-dimensional surface topographical images of the (a)(b)Batch 1 and (c)(d)Batch 2 processed by (a)(c)imperfect spherical and (b)(d)spherical powders.

The densities of the as-built samples were evaluated by the Archimedes method. The density of the as-built samples as a function of the applied volume energy is shown in Fig. 4. It is shown that in the initial stage, the density of the samples built with both kinds of powders increased when increasing energy input. Then, as the volume energy continued to increase, the density reached a stable value. Based on the approximate curve, when the volume energy increased to 39.245 J/mm^3, the density of the samples built with the imperfect spherical powders tended to the stable value of 8.20 g/cm^3; while the density of the samples built with the spherical powders reached the stable value of 8.27 g/cm^3 when the volume energy increased to 22.967 J/mm^3. The imperfect spherical powders required more energy than the spherical powders in order to reach stable values of density, indicating that the energy absorption rate of the imperfect spherical powders was lower than that of the spherical powders. Importantly, the densities of the samples built with the spherical powders were higher than that of the imperfect spherical powders within the entire range of volume energy variation. These results were consistent with the study conducted by Zhong et al. [31]. Accordingly,

under the same processing conditions, the dependence of the defect suppression on the characteristics of the powder feedstocks was particularly highlighted.

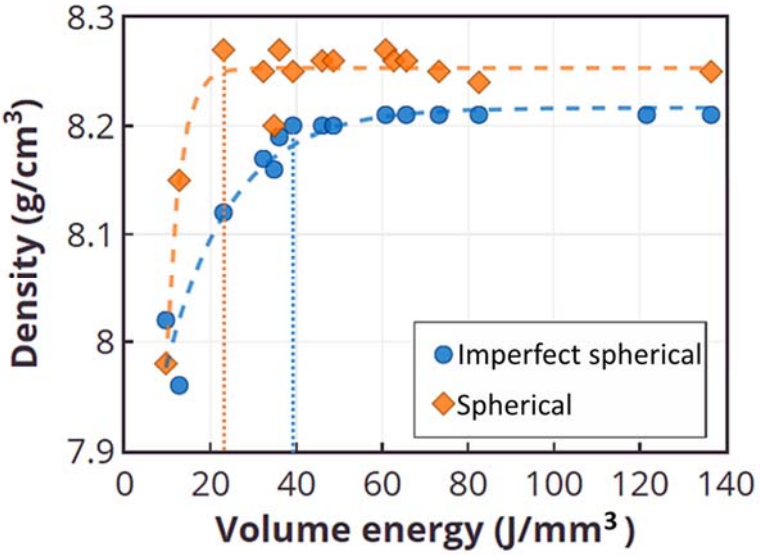

Fig. 4. Variation of the sample density with applied volume energy. For reaching their respective stable values of density, imperfect spherical powders required more energy than spherical powders

3.2 Process windows

Figure 5 shows the process maps for both types of powders, depending on the above characterization of forming quality. In this figure, from the bottom right to the top left, the energy input varies from low to high. The samples with a density below 8.19 g/cm^3 were classified as porous (low density due to insufficient energy absorption) and marked by blue dots. The samples with an arithmetical mean roughness (Sa) of 0.7 mm or more were defined as uneven (inferior surface topography caused by excessive melting) and represented by red dots. The samples with Sa less than 0.7 mm and a density of 8.19 g/cm^3 or more were dense & even (high density and excellent surface topography) and marked by green dots. There were fewer green spots for samples built with the imperfect spherical powders than that for the samples built with the spherical powders, which showed that processing with the spherical powders had a relatively broad process window (region covered by the green band), ensuring forming quality. Irrespective of whether the energy input tended to be insufficient or excessive, the spherical powders showed better adaptability than that of the imperfect spherical powders.

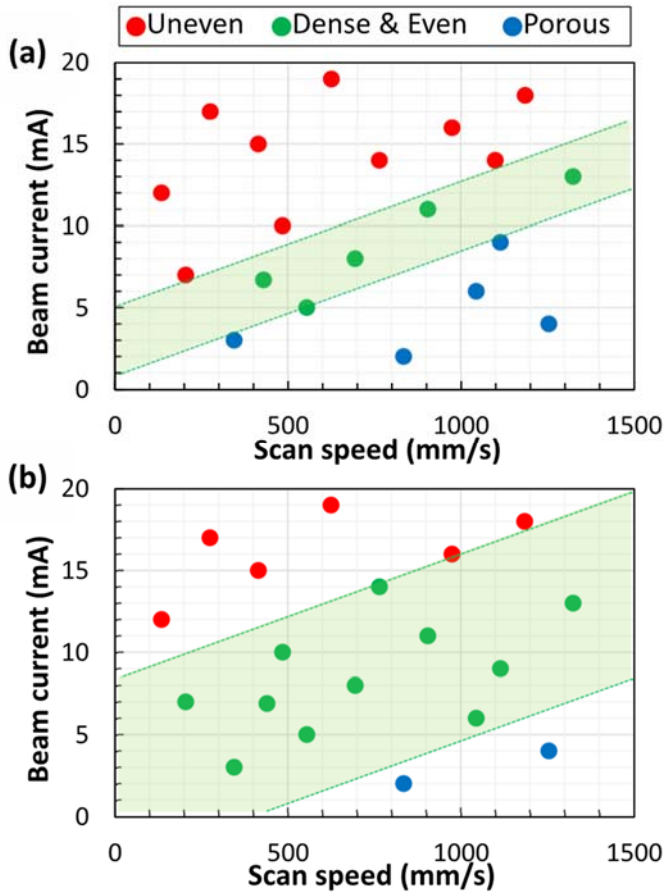

Fig. 5. Process maps for fabrication by (a)imperfect spherical and (b)spherical powders, depending on the characterization of forming quality.

3.3 Internal defects

Generally, the most suitable processing parameters vary depending on powder types. In order to further clarify the influence of powder characteristics (i.e., built-in defects and particle geometry) on the forming quality, it is necessary to obtain the optimal processing conditions for the imperfect spherical and spherical powders. Based on the relationship between the processing parameters and surface topography presented above, the optimal processing conditions for the imperfect spherical and spherical powders were obtained through a simple machine learning-based approach proposed by Aoyagi et al. [32]. The approach was developed using a support vector machine to construct a process map for AM. By classifying the samples to be good or bad in surface topography, the optimal conditions ensuring forming quality were determined. Figure 6(a) and (b) shows the constructed process map as a function of beam current and scan velocity. The color represents the value of the decision function that possesses a physical meaning of the distance from the boundary between the

good and bad conditions. The deepest blue in the contour plots corresponds to the optimal processing condition. The beam currents of 6.7 and 6.9 mA and the scan velocities of 430 and 440 mm/s were the optimal parameters for the imperfect spherical and spherical powders, respectively.

Figure 6(c) and (d) show the three-dimensional surface topographical images of the samples under the optimal processing conditions. The surface roughness of Sa was 39 and 30 μm for the sample built with the imperfect spherical and spherical powders, respectively. The imperfect spherical powders with satellite particles increased the friction, decreased flowability while easily causing inconsistent spreading of the powder bed and, subsequently, of the inferior surface roughness, compared to the spherical powders [33]. The SEM micrographs and corresponding binarized images of the cross section parallel to the building direction are shown in Fig. 7. The density was 8.2 and 8.4 g/cm^3 for the sample built with the imperfect spherical and spherical powders, respectively. Thus, even with the optimal processing conditions, the forming quality of the sample built with the imperfect spherical powders was inferior to the sample built with the spherical powders.

As shown in Fig. 7, there were defects in the sample built with the imperfect spherical powders, namely, gas pore and void. Spherical gas pore with large size came from the powders. These built-in pores result from the gas entrapment during the GA process [34], which can deteriorate the fatigue performance [35][36] and tensile properties [37] of AM-built parts. The large-size gas pores were absent in the sample built with the spherical powders. In addition, the formation of the gas pore with a small size (less than 5 μm) was caused by the escaping of the dissolved gas in the powder during the melting process [38]. Because of the gas jet in the fabrication of imperfect spherical powders, the content of dissolved gas (nitrogen in Table 1) was much larger than that in the spherical powders. Accordingly, there were more small-size pores in the sample built with the imperfect spherical powders than in the sample built with the spherical powders.

It is worth noting that there were some elongated irregularly shaped voids in the sample built with the imperfect spherical powders. These voids arranged along the building direction and were distributed in the interdendritic region. Such kind of interdendritic void was almost absent in the sample built with the spherical powders. It is considered to be caused by inappropriate melting and solidification conditions in the local region and could act as the crack initiation [36] during service of a component.

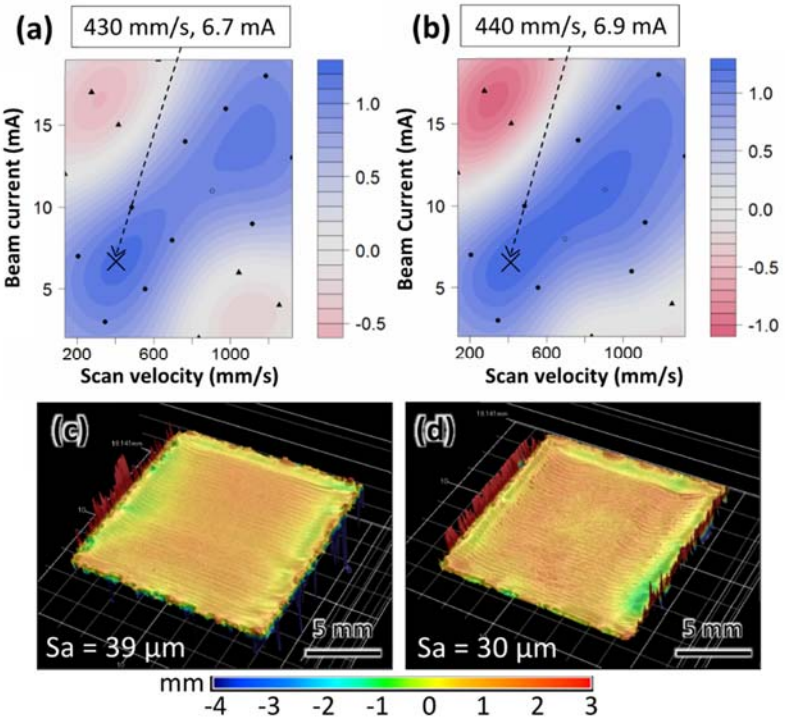

Fig. 6. (a)(b)Constructed process maps derived by a machine learning method as a function of beam current and scan velocity. Three-dimensional surface topographical images of the samples built with (a)(c)imperfect spherical and (b)(d)spherical powders under optimal processing conditions.

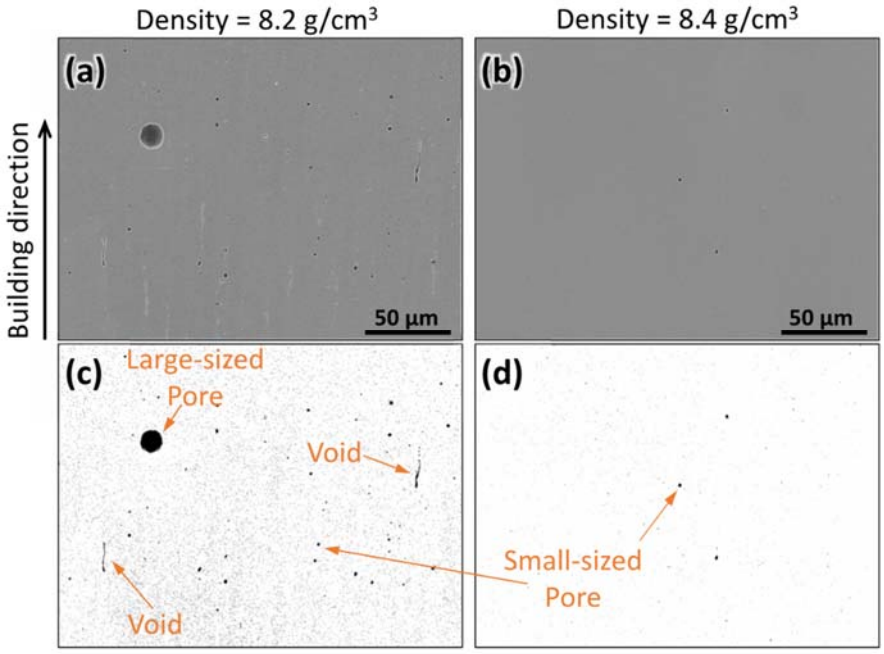

Fig. 7. (a)(b)SEM micrographs and (c)(d)corresponding binarized images of the cross section parallel to the building direction. Even under optimal processing conditions, the sample built with (a)(c)imperfect spherical powders exhibited higher porosity than the sample built with (b)(d)spherical powders.

4. Discussion

4.1 On the role of powder characteristics in the process window

Seen from the results shown in Section 3.1, the samples built with the imperfect spherical powders were likely to exhibit porous morphological features caused by lack–of–fusion and surface unevenness caused by excessive melting under low and high energy input conditions, respectively. Since the processing conditions were the same, the results under low energy input conditions indicated that the energy absorption rate of the imperfect spherical powders was lower than that of the spherical powders. Moreover, the results under high energy input conditions demonstrated that the heat dissipation rate of the imperfect spherical powders was also lower than that of the spherical powders. In other words, the inappropriate fusions were aroused by the powder characteristics. The two types of powders differ significantly in powder morphology that may affect the interaction between the electron beam and the powder layer.

The numerical simulation helped to analyze the consolidation of the powder layer. Powder bed generation was simulated through the DEM model. In the DEM simulation, used for modeling the dynamics of non-spherical powder with attaching satellite particles and irregularly shape, the particle clumping method [39], by which rigid aggregate of individual particles can be created, was applied. Particles within the rigid aggregation can overlap if interforce is released before the simulation starts [24]. Additionally, the DEM simulation helps to satisfy the roundness of a clump or roundness coefficient of a packing. In the present study, the circularity of powder in 2D SEM images was taken to approximate the roundness. As shown in Fig. 8(a) and (b), by using the two types of predefined particle clumping (i.e., powder with satellite particles and elongated particles) and then the adjustment of their fractions (20% and 45%) for circularity matching with the experimental circularity, the DEM model of the imperfect spherical powders (Fig. 8(d)) with the predefined PSD was created. After powder raking, single-layered powder beds were generated. The geometrical data of the powder layer obtained from the DEM simulation then acted as the computational domain for the CtFD simulations of EB melting. As the topology of individual powder particle has been resolved, the temperature-dependent physical properties of solid material (rather than effective properties of porous media) were assigned to powder bed. The contact areas between particles that

can influence the thermal conduction were partially dependent on the mesh resolution of the modeling itself. A mesh size of 5 μm that was smaller enough than the powder size (even the satellite particles), was adopted in the CtFD computational domain.

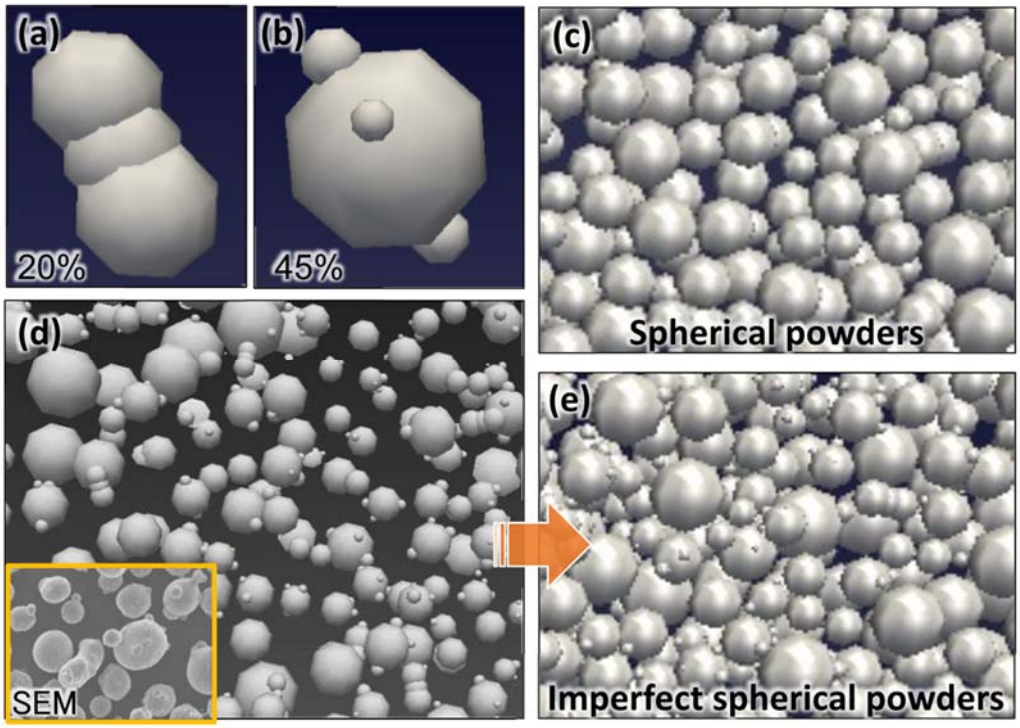

Fig. 8. By using the (a)(b)two types of predefined particle clumping and then the adjustment of their fractions for circularity matching with the experimental circularity, (d)imperfect spherical powders were created and possessed the predefined PSD. After powder raking, single-layered powder beds consisting of (c)spherical and (e)imperfect spherical powders were generated.

From the CtFD simulated melt track profiles shown in Fig. 9, under the same processing condition and the same domain dimension, a more uneven surface profile was observed for the imperfect spherical power layer compared with that for the spherical powder layer. Though the unevenness of the imperfect spherical powder layer was not particularly significant in the case of a single layer, such inferior features in each melt track will inevitably result in undesirable product quality after track-by-track and layer-by-layer EB-PBF building process. The experimentally determined surface profiles after single-track melting are shown in Fig. 10(a) and (b), which illustrated a good agreement with the simulation results. Moreover, as the scan speed was further increased (Fig. 10(c) and (d)), balling and segmentation of melt track occurred for the imperfect

spherical powder layer, which also indicated a narrower process window than that for spherical powders.

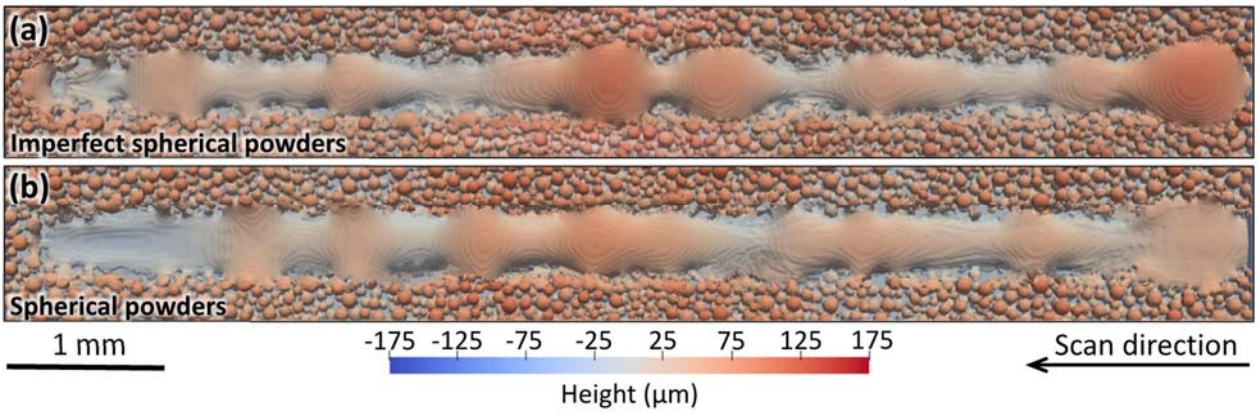

Fig. 9. CtFD simulated melt track profiles on (a)imperfect spherical and (b)spherical powders. Processing condition: beam current = 6 mA, scan speed = 1000 mm/s.

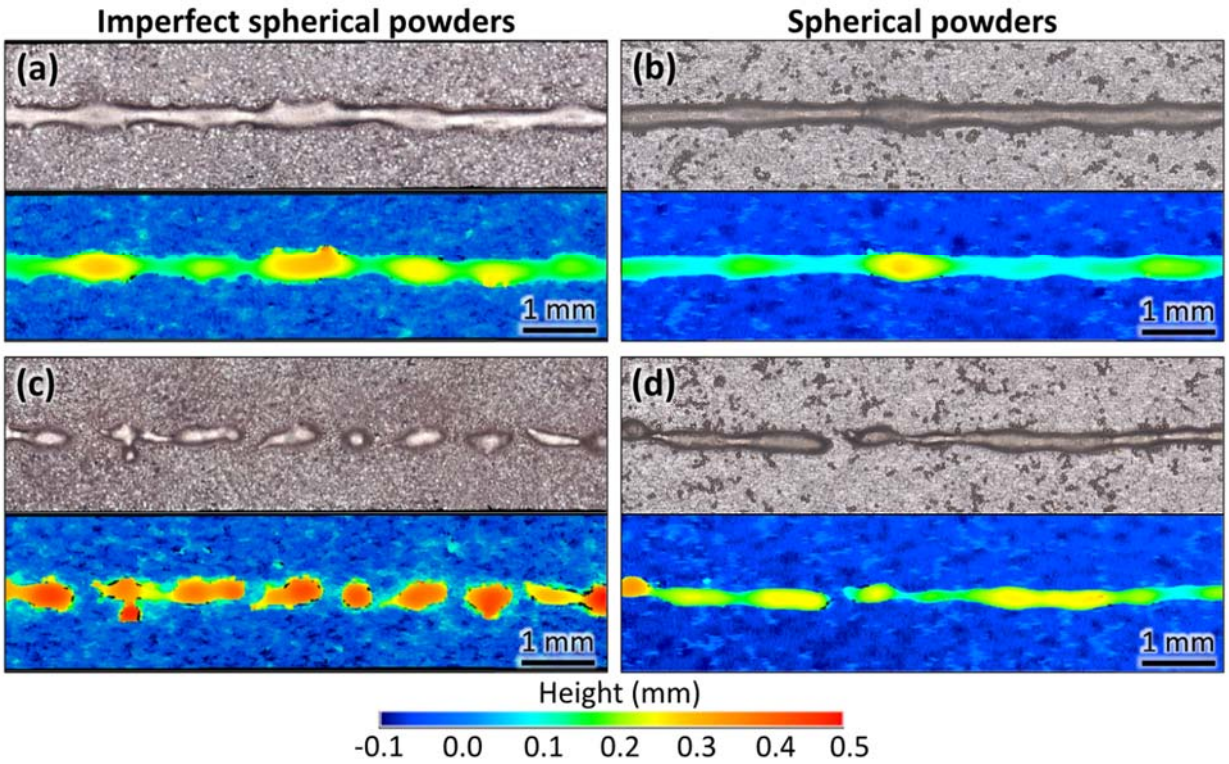

Fig. 10. Experimentally determined surface profiles for (a)(c)imperfect spherical and (b)(d)spherical powder layers after single-track melting. Processing condition: (a)(b)beam current = 6 mA, scan speed = 1000 mm/s; (c)(d) beam current = 6 mA, scan speed = 1500 mm/s.

During the interaction between the EB and the powder bed, the heat transfer conditions of the powder layer determine the melting behavior. On one hand, Fig. 11(a) demonstrates the molten pool

volume of the simulated melt track (Fig. 9) with the fusion process progressing. The molten pool volume of the fusion on the imperfect spherical powder layer was smaller than that on the spherical powder layer, which indicated that the imperfect spherical powder layer was relatively weak in terms of energy absorption. On the other hand, the average temperature change rate of the computational domain (Fig. 11(b)) of the fusion on the imperfect spherical powder layer was also lower than that on the spherical powder layer, which reflected that the imperfect spherical powder layer was also inferior in terms of thermal conductivity. According to the Stefan–Boltzmann law, the power emitted through heat radiation P_{rad} determines the resultant power absorbed by the powder bed P_{bed}:

$$P_{\mathrm{bed}} = \xi P - \varepsilon_{\mathrm{bed}} \sigma A {T_{\mathrm{s}}}^4, \tag{1}$$

where ξ is the energy absorption efficiency; P is the EB power; $\varepsilon_{\mathrm{bed}}$ is the emissivity of the powder bed; σ is the Stefan-Boltzmann constant; A is the surface area; and T_{s} is the surface temperature. Being different from the laser-PBF in which laser reflection occurs, and the unabsorbed energy due to reflected heat flux depends on the deviation angle between the incident ray and surface normal [40], in the EB-PBF, electrons are nearly completely absorbed at the first contacting position with the powder and penetrate material so that electron-beam heating is not sensitive to surface morphology [41][42]. Thus, numerical modeling did not take reflection into account, and ξ was assumed to be a constant in the present study. The emission from the packed powder layer consists of the emission induced from the heated particles and the holes among the packed powder [43]:

$$\varepsilon_{\mathrm{bed}} = A_{\mathrm{h}}\, \varepsilon_{\mathrm{h}} + (1 - A_{\mathrm{h}}) \varepsilon_{\mathrm{s}}, \tag{2}$$

where ε_{s} is the emissivity of the solid material. A_{h} is the area fraction of the surface which is occupied by the radiation-emitting holes and ε_{h} is the effective emissivity of the holes [44]:

$$A_{\mathrm{h}} = \frac{0.908\phi^2}{1.908\phi^2 - 2\phi + 1}, \qquad \varepsilon_h = \frac{\varepsilon_{\mathrm{s}} \left[2 + 3.082 \left(\frac{1-\phi}{\phi}\right)^2\right]}{\varepsilon_{\mathrm{s}} \left[1 + 3.082 \left(\frac{1-\phi}{\phi}\right)^2\right] + 1}, \tag{3}$$

The surface area A and fractional packing porosities ϕ of the powder layers within the computational domains are shown in Table 3, which lists the variables related to the heat radiation of the powder bed. Even though the calculated $\varepsilon_{\mathrm{bed}}$ for the imperfect spherical powder layer was smaller than that for the spherical powder layer, the large surface area A for the imperfect spherical powder layer made the product $\varepsilon_{\mathrm{bed}} \cdot A$ larger than that for the spherical powder layer. Moreover, before the powder layer was completely melted, the simulated average temperature of the surface

under EB irradiation T_s for the imperfect spherical powder layer was also slightly higher than that for the spherical powder layer, which should be caused by the different thermal conductivities; this will be discussed in the following section. Thus, under the same beam diameter and power of the EB irradiation, compared to that of the spherical powder layer, the imperfect spherical powder layer with satellite particles and the resultant large surface area possessed intense heat radiation, thereby reducing the effective energy absorption (Eq. (1)). In addition, for porous material with complexly connected pores, such as a powder bed, thermal conductivity κ_{porous} decreases with increasing porosity ϕ [45]:

$$\kappa_{\text{porous}} = \kappa_{\text{solid}}(1-\phi)^3. \quad (4)$$

Spherical particles possess the highest packing density than other forms of particles [46][47]. In addition to the heat dissipation to the solid in the vertical direction, during the fusion process the heat dissipation to the powder layer in the lateral direction was also significant. Thus, the imperfect spherical powder layer had a high porosity, which reduced the thermal conductivity and restrained the heat dissipation throughout the powder bed during melting. Subsequently, processing with the imperfect spherical powders was easy to cause excessive melting under high energy conditions.

Table 3 Variables related to the heat radiation of the (i) imperfect spherical and (ii) spherical powder layers.

	A	ϕ	ε_s	ε_{bed}	$\varepsilon_{\text{bed}} \cdot A$	T_s
(i)	46.853 cm^2	0.692	0.32	0.5098	23.89	1966 K
(ii)	38.329 cm^2	0.649		0.5145	19.72	1942 K

Due to the different powder morphologies, the surface area and porosity of the powder layers were different, thereby giving rise to different heat transfer properties of the two types of powder layers. Low energy absorption rate and thermal conductivity made the imperfect spherical powders likely to evoke lack–of–fusion and excessive melting under low and high energy conditions, respectively. Thus, in the present study, processing with the spherical powders had a broader process window than the imperfect spherical powders for the EB-PBF-built IN718.

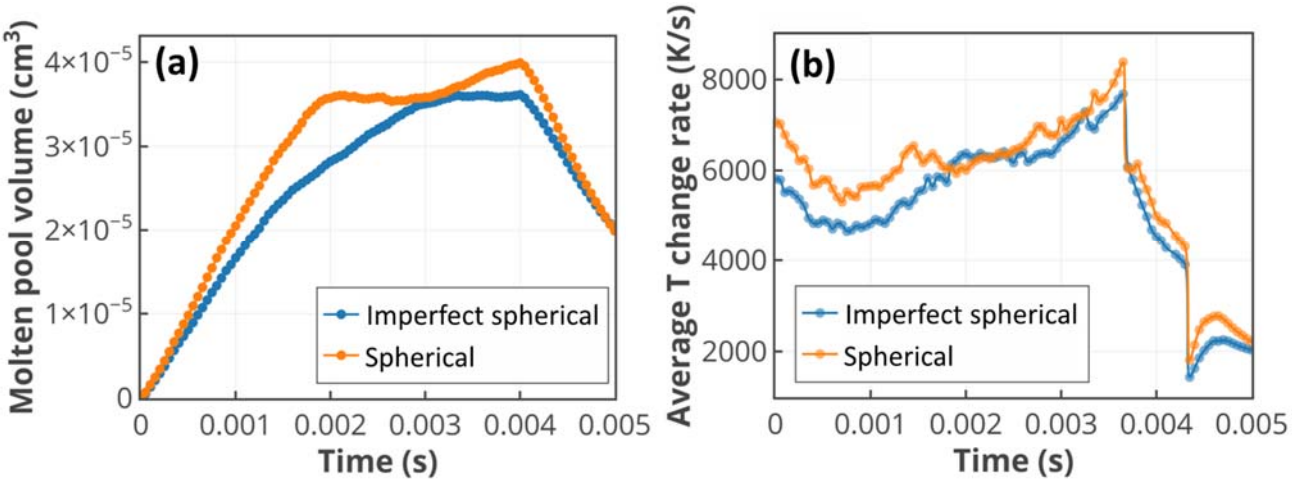

Fig. 11. (a) Molten pool volume and (b) average temperature change rate of the computational domain of the simulated melt track with the fusion process progressing.

4.2 On the role of powder characteristics in internal defect

In terms of internal defects, besides the small- and large-size gas pores that are formed because of the gas entrapment, there were some irregularly shaped voids in the sample built with the imperfect spherical powders. Under the optimal processing conditions shown in Section 3.3, Fig. 12 shows the BSE micrographs of the cross section parallel to the building direction. Due to the specific heat flow and epitaxial growth in AM, the [001] growth direction of dendrite was substantially parallel to the building direction. In particular, the voids in Fig. 12(a) and (c), like the precipitate's chains, arranged along the building direction and were distributed at the interdendritic region. Generally, these voids are considered as the interdendritic shrinkage that resulted from insufficient liquid feeding into the interdendritic channels during solidification. The schematic diagram in Fig. 13(a) shows that the higher the cooling rate, the more limited the dendrite length, which is conducive to the inflow of the interdendritic liquid, thereby preventing the occurrence of shrinkage [48].

In addition, during the solidification process, the tendency of shrinkage formation is influenced by the densities of the solid phase ρ_s and the liquid phase ρ_l of an alloy [49], which can be expressed as

$$Shrinkage = \frac{\rho_s - \rho_l}{\rho_s}. \quad (5)$$

Thus, the more significant the density difference between solid and liquid phases, the more efficiently the shrinkage occurs. The chemical composition of the liquid phase determines its density.

As shown in Fig. 12(e) and (f), in the sample built with the imperfect spherical powder, MC carbide-(Nb, Ti)C and Laves phase-$(Ni, Cr)_2(Nb, Ti)$ presented in the interdendritic regions due to the solidification microsegregation. In particular, the densities of the principal constituent elements (Nb, Ti, Cr, C) of these two interdendritic phases are all lower than that of the matrix element Ni, which means that the density difference between solid and liquid phases at the solidification front increases when increasing solute concentration. Alternatively stated, the great segregation degree of these elements into the interdendritic region promotes the possibility of interdendritic shrinkage. Importantly, for an alloy with a specific composition, the microsegregation degree is determined by the solidification conditions. The solute enrichment of the liquid phase decreases with an increasing solidification rate [50]. During the rapid solidification with a high solidification rate involved in EB-PBF, solute trapping tends to occur when it is difficult for the solute to have enough time to diffuse into the liquid phase. As shown in the schematic diagram of Fig. 13(b), under a high solidification rate, segregation is suppressed, so that the concentration difference or density difference between the solid and liquid phase is reduced, thereby reducing the tendency of interdendritic shrinkage formation.

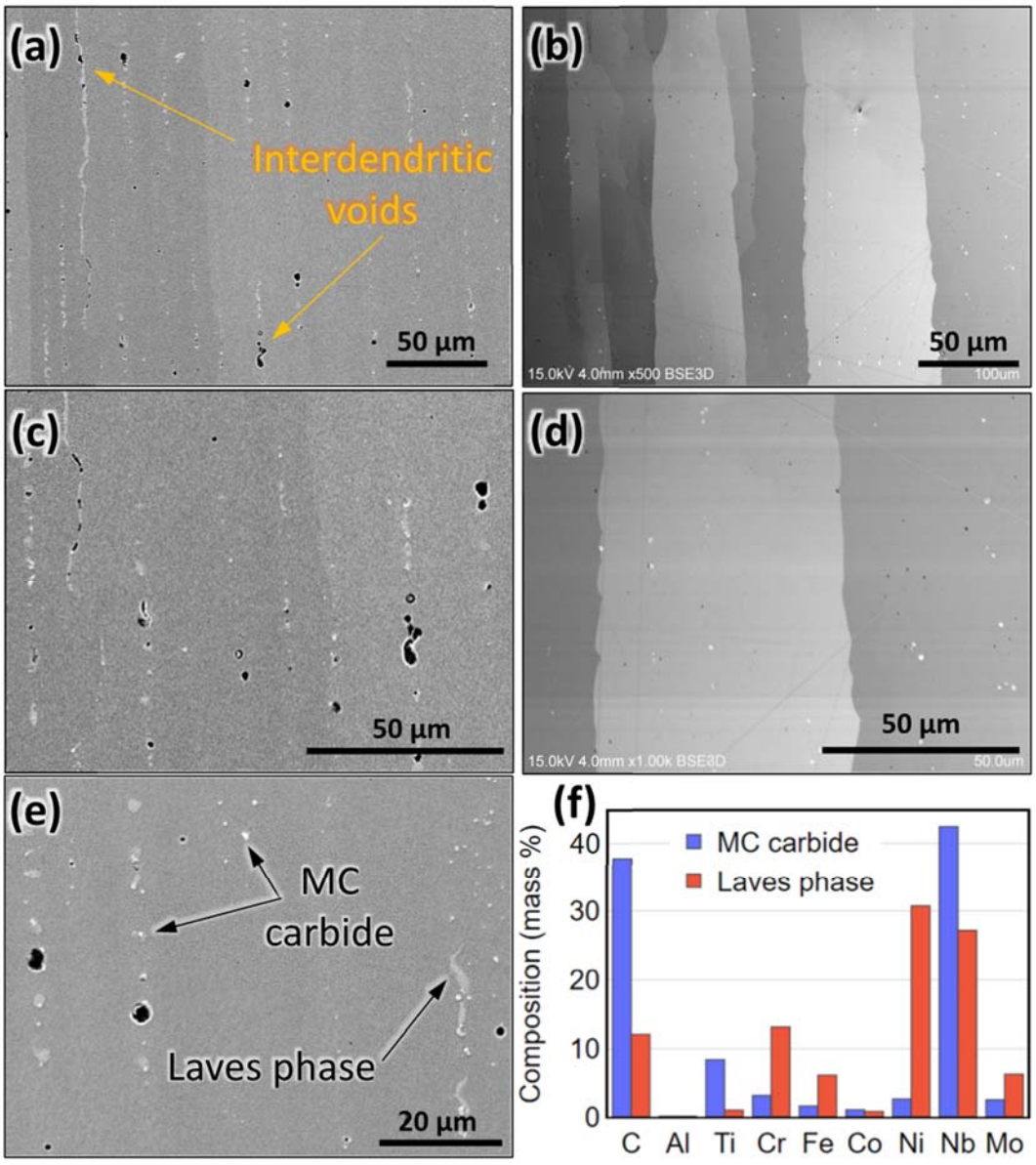

Fig. 12. BSE micrographs of the cross section parallel to the building direction under optimal processing conditions. (a)(c)In the sample built with imperfect spherical powders, the voids arranged along the building direction and distributed at the interdendritic region. (b)(d)Such interdendritic voids hardly appear in the sample built with spherical powders. (e)(f)MC carbide and Laves phase presented in the interdendritic regions due to the solidification microsegregation.

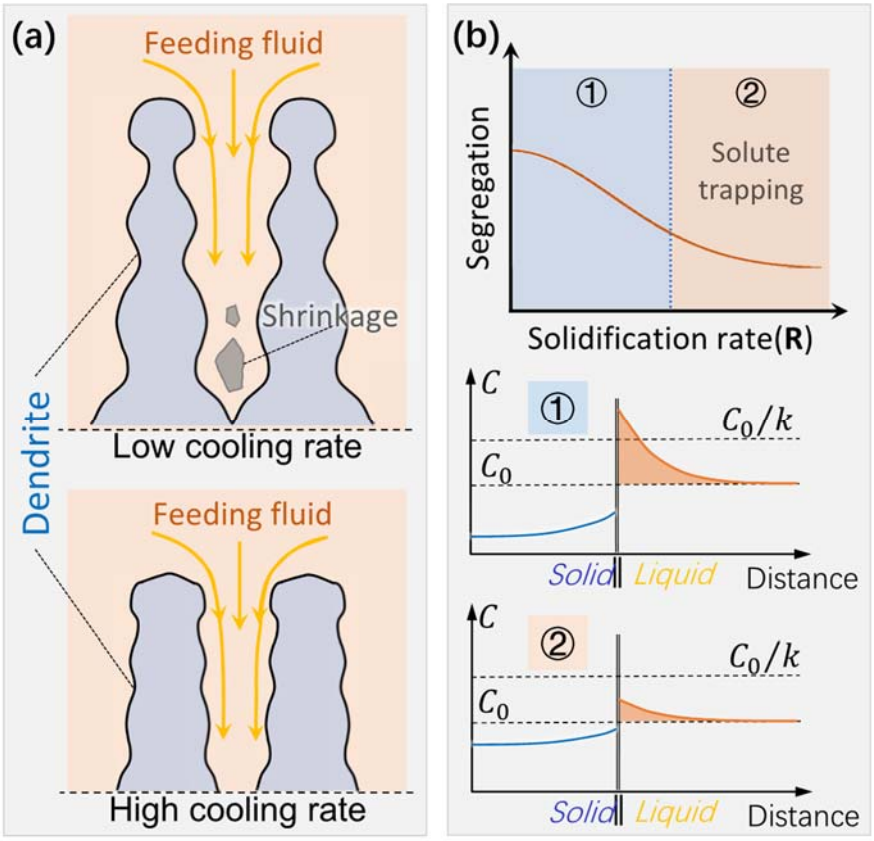

Fig. 13. (a)Schematic diagram shows that the higher the cooling rate, the more limited the dendrite length, which is conducive to the inflow of the interdendritic liquid, thereby preventing the occurrence of shrinkage. (b)Schematic diagram shows that under a high solidification rate, segregation is suppressed so that the concentration difference or density difference between the solid and liquid phase is reduced, thereby reducing the tendency of interdendritic shrinkage formation.

Notably, such interdendritic voids hardly appeared in the sample built with the spherical powders (Fig. 12(b) and (d)). Moreover, the amount of interdendritic precipitates in the sample built with the spherical powders was much less than that in the sample built with the imperfect spherical powders. The different characteristics shown in the samples built with the two types of powders indicated that the solidification conditions were different after melting. Under the same processing condition, Fig. 14(a) illustrates the simulated solidification parameters at solidification fronts that were derived following the principles and methods in a previous study [27]. As shown in Fig. 14(a), fusion on the spherical powder layer exhibited a higher solidification rate (R) and resultant higher cooling rate ($G \times R$) than that on the imperfect spherical powder layer. The molten pool geometry determines the spatial relationship between scan speed (V) and R. Due to the high energy absorption rate, the fusion

on the spherical powder layer produced a deeper molten pool than the imperfect spherical powder layer (Fig. 14(b)). The schematic diagram in Fig. 14(c) shows that under a given EB scan speed (molten pool translation speed), a deep molten pool creates a small angle between V and R ($R = V \cdot \cos\theta$), and subsequently, a large R. Therefore, the suppression of interdendritic voids forming in the sample built with the spherical powder was due to the high cooling rate and solidification rate. As a result, the liquid phase easily flowed into the interdendritic region to compensate voids, and the insignificant segregation tendency made the solid and liquid densities closer, which in turn, resisted at interdendritic shrinkage formation.

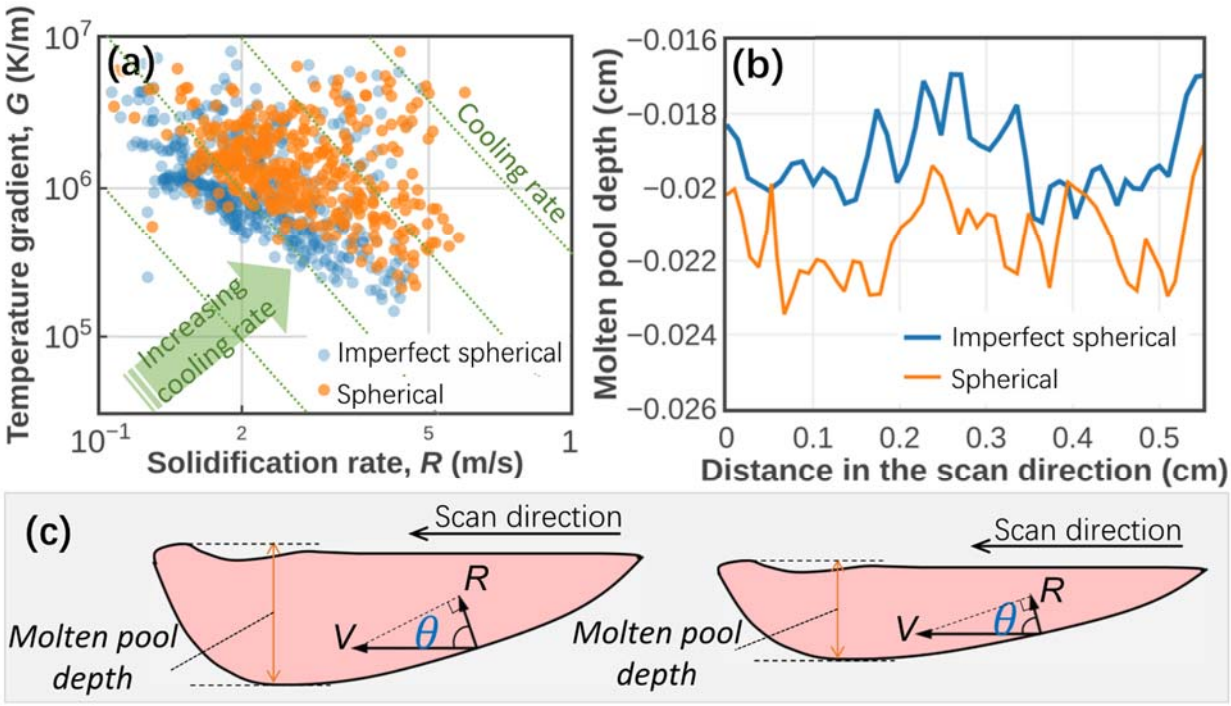

Fig. 14. (a) Simulated solidification parameters at solidification fronts. (b) Owing to the high energy absorption rate, the fusion on the spherical powder layer produced a deeper molten pool than the imperfect spherical powder layer. (c) Schematic diagram shows that under a given EB scan speed (molten pool translation speed), a deep molten pool creates a small angle between V and R, and subsequently, a large R.

5. Conclusions

The forming qualities, in terms of surface topography, density, and internal defect, were characterized for Inconel 718 samples fabricated by EB-PBF using the (i) imperfect spherical and (ii)

spherical powders powder feedstocks. The significance of powder characteristics in defect suppression was clarified with the aid of mesoscale numerical simulations. The main conclusions are summarized as follows:

1) The samples built with the imperfect spherical powders were likely to exhibit porous morphological features of lack−of−fusion and surface unevenness caused by excessive melting under low and high energy input conditions, respectively.
2) Processing with the spherical powders had a relatively broad process window suppressing defect. Irrespectively on whether the energy input tended to be insufficient or excessive, the spherical powders showed better adaptability than the imperfect spherical powders.
3) Even with the optimal processing condition derived by a machine learning method, the forming quality of the sample built with the imperfect spherical powders was inferior to the sample built with the spherical powders. Besides spherical gas pores formed by the gas entrapment of the powder fabrication, there were a lot of interdendritic voids in the sample built with the imperfect spherical powders.
4) Due to the different particle morphologies between the two types of powders, the surface area and porosity of the packed powder layers were different, thereby giving rise to different heat transfer properties. Low energy absorption rate and thermal conductivity made the imperfect spherical powders likely to evoke lack–of–fusion and excessive melting under low and high energy conditions, respectively.
5) The suppression of interdendritic voids forming in the sample built with the spherical powders was due to the high cooling and solidification rates. As a result, the liquid easily flowed into the interdendritic region to compensate voids, and the insignificant segregation tendency made the solid and liquid densities closer, which in turn, resisted at interdendritic shrinkage formation.

Acknowledgments

This work was supported by the Japan Ministry of Economy, Trade and Industry (METI); the New Energy and Industrial Technology Development Organization (NEDO); the Technology Research Association for Future Additive Manufacturing (TRAFAM). We would like to thank Editage (www.editage.com) for English language editing.

References

[1] C. Körner, Additive manufacturing of metallic components by selective electron beam melting - A review, International Materials Reviews. 61 (2016) 361–377. doi:10.1080/09506608.2016.1176289.

[2] M. Galati, L. Iuliano, A literature review of powder-based electron beam melting focusing on numerical simulations, Additive Manufacturing. 19 (2018) 1–20. doi:10.1016/j.addma.2017.11.001.

[3] P. Nandwana, M.M. Kirka, V.C. Paquit, S. Yoder, R.R. Dehoff, Correlations Between Powder Feedstock Quality, In Situ Porosity Detection, and Fatigue Behavior of Ti-6Al-4V Fabricated by Powder Bed Electron Beam Melting: A Step Towards Qualification, JOM. 70 (2018) 1686–1691. doi:10.1007/s11837-018-3034-6.

[4] Z. Snow, R. Martukanitz, S. Joshi, On the development of powder spreadability metrics and feedstock requirements for powder bed fusion additive manufacturing, Additive Manufacturing. 28 (2019) 78–86. doi:10.1016/j.addma.2019.04.017.

[5] M.J. Heiden, L.A. Deibler, J.M. Rodelas, J.R. Koepke, D.J. Tung, D.J. Saiz, B.H. Jared, Evolution of 316L stainless steel feedstock due to laser powder bed fusion process, Additive Manufacturing. 25 (2019) 84–103. doi:10.1016/j.addma.2018.10.019.

[6] N. Aboulkhair, N, Maskery, I, Ashcroft I, Tuck, C, Everitt, The role of powder properties on the processability of Aluminium alloys in selective laser melting Lasers in Manufacturing Conference 2015 The role of powder properties on the processability of Aluminium alloys in selective laser melting, in: Lasers in Manufacturing Conference 2015, 2015.

[7] J. Karlsson, A. Snis, H. Engqvist, J. Lausmaa, Characterization and comparison of materials produced by Electron Beam Melting (EBM) of two different Ti-6Al-4V powder fractions, Journal of Materials Processing Technology. 213 (2013) 2109–2118. doi:10.1016/j.jmatprotec.2013.06.010.

[8] C. Panwisawas, C.L. Qiu, Y. Sovani, J.W. Brooks, M.M. Attallah, H.C. Basoalto, On the role of thermal fluid dynamics into the evolution of porosity during selective laser melting, Scripta Materialia. 105 (2015) 14–17. doi:10.1016/j.scriptamat.2015.04.016.

[9] W. Tillmann, C. Schaak, J. Nellesen, M. Schaper, M.E. Aydinöz, K.P. Hoyer, Hot isostatic pressing of IN718 components manufactured by selective laser melting, Additive Manufacturing. 13 (2017) 93–102. doi:10.1016/j.addma.2016.11.006.

[10] R. Cunningham, A. Nicolas, J. Madsen, E. Fodran, E. Anagnostou, M.D. Sangid, A.D. Rollett, Analyzing the effects of powder and post-processing on porosity and properties of electron beam melted Ti-6Al-4V, Materials Research Letters. 5 (2017) 516–525. doi:10.1080/21663831.2017.1340911.

[11] S. Sui, H. Tan, J. Chen, C. Zhong, Z. Li, W. Fan, A. Gasser, W. Huang, The influence of Laves phases on the room temperature tensile properties of Inconel 718 fabricated by powder feeding laser additive manufacturing, Acta Materialia. 164 (2019) 413–427. doi:10.1016/j.actamat.2018.10.032.

[12] L. Scime, J. Beuth, Melt pool geometry and morphology variability for the Inconel 718 alloy in a laser powder bed fusion additive manufacturing process, Additive Manufacturing. 29 (2019). doi:10.1016/j.addma.2019.100830.

[13] X. Wang, K. Chou, Effects of thermal cycles on the microstructure evolution of Inconel 718 during selective laser melting process, Additive Manufacturing. 18 (2017) 1–14. doi:10.1016/j.addma.2017.08.016.

[14] G.L. Knapp, N. Raghavan, A. Plotkowski, T. DebRoy, Experiments and simulations on solidification microstructure for Inconel 718 in powder bed fusion electron beam additive manufacturing, Additive Manufacturing. 25 (2019) 511–521. doi:10.1016/j.addma.2018.12.001.

[15] J.H. Tan, W.L.E. Wong, K.W. Dalgarno, An overview of powder granulometry on feedstock and part performance in the selective laser melting process, Additive Manufacturing. 18 (2017) 228–255. doi:10.1016/j.addma.2017.10.011.

[16] L.I. Escano, N.D. Parab, L. Xiong, Q. Guo, C. Zhao, K. Fezzaa, W. Everhart, T. Sun, L. Chen, Revealing particle-scale powder spreading dynamics in powder-bed-based additive manufacturing process by high-speed x-ray imaging, Scientific Reports. 8 (2018) 1-11F. doi:10.1038/s41598-018-33376-0.

[17] P. Sun, Z.Z. Fang, Y. Zhang, Y. Xia, Review of the Methods for Production of Spherical Ti and Ti Alloy Powder, JOM. 69 (2017) 1853–1860. doi:10.1007/s11837-017-2513-5.

[18] A. Bauereiß, T. Scharowsky, C. Körner, Defect generation and propagation mechanism during additive manufacturing by selective beam melting, Journal of Materials Processing Technology. 214 (2014) 2522–2528. doi:10.1016/j.jmatprotec.2014.05.002.

[19] N.T. Aboulkhair, N.M. Everitt, I. Ashcroft, C. Tuck, Reducing porosity in AlSi10Mg parts processed by selective laser melting, Additive Manufacturing. 1 (2014) 77–86. doi:10.1016/j.addma.2014.08.001.

[20] B. Dutta, S. Babu, B. Jared, Science, Technology and Applications of Metals in Additive Manufacturing, 1st Editio, Elsevier, Amsterdam, 2019.

[21] G. Chen, S.Y. Zhao, P. Tan, J. Wang, C.S. Xiang, H.P. Tang, A comparative study of Ti-6Al-4V powders for additive manufacturing by gas atomization, plasma rotating electrode process and plasma atomization, Powder Technology. 333 (2018) 38–46. doi:10.1016/j.powtec.2018.04.013.

[22] C.M. Huang, Y.J. Lee, D.K.J. Lin, S.Y. Huang, Model selection for support vector machines via uniform design, Computational Statistics and Data Analysis. 52 (2007) 335–346. doi:10.1016/j.csda.2007.02.013.

[23] Modenese, C. (2013). Numerical study of the mechanical properties of lunar soil by the discrete element method (Doctoral dissertation, Oxford University, UK).

[24] V. Šmilauer et al. (2015), Yade Documentation 2nd ed. The Yade Project. (http://yade-dem.org/doc/). doi:10.5281/zenodo.34073.

[25] *FLOW-3D*® Version 11.2 [Computer software]. (2017). Santa Fe, NM: Flow Science, Inc. https://www.flow3d.com.

[26] Y. Zhao, Y. Koizumi, K. Aoyagi, K. Yamanaka, A. Chiba, Characterization of powder bed generation in electron beam additive manufacturing by discrete element method (DEM), in: Materials Today: Proceedings, 2017: pp. 11437–11440. doi:10.1016/j.matpr.2017.09.023.

[27] Y. Zhao, Y. Koizumi, K. Aoyagi, D. Wei, K. Yamanaka, A. Chiba, Molten pool behavior and effect of fluid flow on solidification conditions in selective electron beam melting (SEBM) of a biomedical Co-Cr-Mo alloy, Additive Manufacturing. 26 (2019) 202–214. doi:10.1016/j.addma.2018.12.002.

[28] D. Herzog, V. Seyda, E. Wycisk, C. Emmelmann, Additive manufacturing of metals, Acta Materialia. 117 (2016) 371–392. doi:10.1016/j.actamat.2016.07.019.

[29] T. Mukherjee, J.S. Zuback, A. De, T. DebRoy, Printability of alloys for additive manufacturing, Scientific Reports. 6 (2016) 19717. doi:10.1038/srep19717.

[30] W.W. Wits, R. Bruins, L. Terpstra, R.A. Huls, H.J.M. Geijselaers, Single scan vector prediction in selective laser melting, Additive Manufacturing. 9 (2016) 1–6. doi:10.1016/j.addma.2015.12.001.

[31] C. Zhong, J. Chen, S. Linnenbrink, A. Gasser, S. Sui, R. Poprawe, A comparative study of Inconel 718 formed by High Deposition Rate Laser Metal Deposition with GA powder and PREP powder, Materials and Design. 107 (2016) 386–392. doi:10.1016/j.matdes.2016.06.037.

[32] K. Aoyagi, H. Wang, H. Sudo, A. Chiba, Simple method to construct process maps for additive manufacturing using a support vector machine, Additive Manufacturing. 27 (2019) 353–362. doi:10.1016/j.addma.2019.03.013.

[33] W. Nan, M. Pasha, T. Bonakdar, A. Lopez, U. Zafar, S. Nadimi, M. Ghadiri, Jamming during particle spreading in additive manufacturing, Powder Technology. 338 (2018) 253–262. doi:10.1016/j.powtec.2018.07.030.

[34] H. Qi, M. Azer, A. Ritter, Studies of standard heat treatment effects on microstructure and mechanical properties of laser net shape manufactured INCONEL 718, Metallurgical and Materials Transactions A: Physical Metallurgy and Materials Science. 40 (2009) 2410–2422. doi:10.1007/s11661-009-9949-3.

[35] X. Shui, K. Yamanaka, M. Mori, Y. Nagata, K. Kurita, A. Chiba, Effects of post-processing on cyclic fatigue response of a titanium alloy additively manufactured by electron beam melting, Materials Science and Engineering A. 680 (2017) 239–248. doi:10.1016/j.msea.2016.10.059.

[36] N. Hrabe, T. Gnäupel-Herold, T. Quinn, Fatigue properties of a titanium alloy (Ti–6Al–4V) fabricated via electron beam melting (EBM): Effects of internal defects and residual stress, International Journal of Fatigue. 94 (2017) 202–210. doi:10.1016/j.ijfatigue.2016.04.022.

[37] S. Biamino, A. Penna, U. Ackelid, S. Sabbadini, O. Tassa, P. Fino, M. Pavese, P. Gennaro, C. Badini, Electron beam melting of Ti-48Al-2Cr-2Nb alloy: Microstructure and mechanical properties investigation, Intermetallics. 19 (2011) 776–781. doi:10.1016/j.intermet.2010.11.017.

[38] R. Cunningham, S.P. Narra, C. Montgomery, J. Beuth, A.D. Rollett, Synchrotron-Based X-ray Microtomography Characterization of the Effect of Processing Variables on Porosity Formation in Laser Power-Bed Additive Manufacturing of Ti-6Al-4V, JOM. 69 (2017) 479–484. doi:10.1007/s11837-016-2234-1.

[39] E.J.R. Parteli, DEM simulation of particles of complex shapes using the multisphere method: Application for additive manufacturing, in: AIP Conference Proceedings, American Institute of Physics, 2013: pp. 185–188. doi:10.1063/1.4811898.

[40] C.D. Boley, S.A. Khairallah, A.M. Rubenchik, Calculation of laser absorption by metal powders in additive manufacturing, Applied Optics. 54 (2015) 2477. doi:10.1364/ao.54.002477.

[41] C. Körner, A. Bauereiß, E. Attar, Fundamental consolidation mechanisms during selective beam melting of powders, Modelling and Simulation in Materials Science and Engineering. 21 (2013). doi:10.1088/0965-0393/21/8/085011.

[42] H.E. Cline, T.R. Anthony, Heat treating and melting material with a scanning laser or electron beam, Journal of Applied Physics. 48 (1977) 3895–3900. doi:10.1063/1.324261.

[43] S.S. Sih, J.W. Barlow, The Prediction of the Thermal Conductivity of Powders, Proceedings of the Solid Freeform Fabrication Symposium. 22 (1994) 397–401. doi:10.1080/02726350490501682a.

[44] Sih, S. S., & Barlow, J. W. (1995). Emissivity of powder beds. In 1995 International Solid Freeform Fabrication Symposium.

[45] I. Sumirat, Y. Ando, S. Shimamura, Theoretical consideration of the effect of porosity on thermal conductivity of porous materials, Journal of Porous Materials. 13 (2006) 439–443. doi:10.1007/s10934-006-8043-0.

[46] German, R. M., Particle packing characteristics, Princeton, N.J. : Metal Powder Industries Federation, Princeton, N.J, 1989.

[47] Q.B. Nguyen, M.L.S. Nai, Z. Zhu, C.N. Sun, J. Wei, W. Zhou, Characteristics of Inconel Powders for Powder-Bed Additive Manufacturing, Engineering. 3 (2017) 695–700. doi:10.1016/J.ENG.2017.05.012.

[48] D.R. Askeland, W.J. Wright, Essentials of materials science and engineering, fourth ed., Cengage Learning, Boston, 2018.

[49] T. Magnusson, L. Arnberg, Density and solidification shrinkage of hypoeutectic aluminum-silicon alloys, Metallurgical and Materials Transactions A: Physical Metallurgy and Materials Science. 32 (2001) 2605–2613. doi:10.1007/s11661-001-0050-9.

[50] P.K. Galenko, E. V Abramova, D. Jou, D.A. Danilov, V.G. Lebedev, D.M. Herlach, Solute trapping in rapid solidification of a binary dilute system: A phase-field study, Physical Review E - Statistical, Nonlinear, and Soft Matter Physics. 84 (2011) 41143. doi:10.1103/PhysRevE.84.041143.